Proceedings of the ASME 2021 Conference on Smart Materials, Adaptive Structures and Intelligent Systems
SMASIS2021
September 14-15, 2021, Virtual, Online

SMASIS 2021-67508

1D SHAPE MATCHING OF A LITHIUM-ION BATTERY ACTUATOR

Cody Gonzalez[1]
Department of Mechanical Engineering
The Pennsylvania State University
University Park, Pennsylvania 16802
Email: cag46@psu.edu

Shuhua Shan
Department of Mechanical Engineering
The Pennsylvania State University
University Park, Pennsylvania 16802
Email: sxs2472@psu.edu

Mary Frecker
Professor
Department of Mechanical Engineering
The Pennsylvania State University
University Park, Pennsylvania 16802
Email: mxf36@psu.edu

Christopher Rahn
Professor
Department of Mechanical Engineering
The Pennsylvania State University
University Park, Pennsylvania 16802
Email: cdrahn@psu.edu

ABSTRACT

Silicon anodes have been demonstrated to provide significant actuation in addition to energy storage in lithium-ion batteries (LIBs). This work studies the optimization of 1D unimorph and bimorph actuators to achieve a target shape upon actuation. A 1D shape matching with design optimization is used to estimate the varied charge distribution along the length for a LIB actuator and thereby the effect of distance between electrodes in charging.

A genetic algorithm (GA) is used with actuation strain distribution as the design variable. The objective of the optimization is to shape-match by minimizing the shape error between a target shape and actuated shape, both defined by several points along the length.

The approach is experimentally validated by shape matching a notched unimorph target shape. A shape error of 1.5% is obtained. An optimized unimorph converges to an objective function of less than 0.029% of the length at full state of charge (SOC) for a 5-segment beam.

A second shape matching case study using a bimorph is investigated to showcase the tailorability of LIB actuators. The optimal bimorph achieves an objective function of less than 0.23% of the length for a design variable set of top and bottom actuation strain of an 8-segment beam. The actuated shape nearly matches the target shape by simultaneously activating top and bottom active layers to achieve the same differential actuation strain (the difference between top and bottom active layer actuation strain).

The results show that a bimorph actuator can achieve a given shape while also storing significantly more charge than is necessary to maintain a given complex shape. This demonstrates a strength of energy storage based actuators: excess energy can be stored within the actuator and can be expended without affecting the work done or the shape maintained by the actuator.

Keywords: Active materials, modeling, multifunctional materials, bioinspired smart materials

1. INTRODUCTION

1.1. Silicon as a superior anode material

Lithium-ion batteries are a ubiquitous technology that are essential as intermittent renewable energy sources become more prevalent and larger capacity energy storage is needed [1]. Lithium-ion batteries (LIBs) are comprised of positive electrode (cathode) and negative electrode (anode) separated by a lithium-ion porous separator and connected by an electrolyte (in this case liquid electrolyte formed by the dissolution of lithium salts in a solvent) [2]. Silicon has potential as a superior anode to fulfill this need for larger capacity batteries because of its high

[1] Address all correspondence to this author.

theoretical specific capacity (4200 $mAhg^{-1}$, 10 times that of commercial graphite anodes) [3].

Lithiated silicon expands volumetrically over 300% due to alloying with lithium whereas graphite only achieves 13.1% volumetric expansion due to its lithium intercalation method [4,5]. However, by reducing the diameter of silicon nanoparticles below a critical diameter as specified by Liu *et al.*, silicon ceases to pulverize (crack and fracture until electrical contact is lost) [6]. Whereas Chin *et al.* show that a $LiCoO_2$-graphite battery can be successfully used as an actuator with greater strain than piezoelectrics, silicon can be used to achieve even greater actuation strain [4]. Electrochemically based actuation associated with charging in silicon-anode composite based LIBs, has demonstrated on the order of tens of percent actuation strain [7]. Large actuation strain is useful in actuators because it increases actuator metrics such as free deflection, blocked force, and actuator energy.

1.2. Lithium ion batteries as multifunctional actuators

Silicon is also a multifunctional material (functions: energy storage, actuation, sense). Cannarella *et al.* investigated the stress-potential coupling mechanisms that are responsible for silicon's ability to self-sense [8]. Ma *et al.* showed the experimental actuation of a silicon anode based LIB and the resultant stress-potential coupling [9].

The free deflection of silicon anode based unimorph actuators are first modeled by Ma *et al.* [10,11]. The model is extended to predict the free deflection of segmented unimorph actuators by the authors [12] and then predict the blocked force (force necessary to achieve zero tip deflection) to extend the case studies and predict additional actuator metrics [7,12,13]. Bimorph LIB actuation free deflection is also predicted [14]. Segmented actuators are defined here as a series of electrically isolated, mechanical connected LIB segments that can be independently controlled and maintain separate states of charge (SOC) [7].

1.3. Shape matching and design optimization

Shape matching for segmented actuators in general is motivated by the possibility of intelligently designing a segmented actuator to achieve a particular shape or pattern. By seeking to optimize for a particular target shape, several design variables can be chosen, including segment thickness, state of charge (SOC) of a given active layer, and differential state of charge (the difference between SOC of the upper and lower active layer of a bimorph configuration).

As applied to a segmented actuator, shape matching allows for the achievement of a particular shape with minimal shape error, and potentially minimum energy expenditure or minimum stiffness. Shape matching may be defined as a form of design optimization, where a given design is optimized to minimize the shape error between an actuated design shape and a target shape while satisfying given constraints.

Design optimization is particularly useful in a LIB actuator, where it can be used to match a target shape for a minimum SOC (and resulting actuation strain) per segment, for a given geometric thickness or elastic modulus. The design optimization of a LIB actuator could allow for achieving a particular shape without external loading. This would allow for more useful work to be done when an external force is applied. For example, as a smart LIB actuator wraps around a limb to apply a uniform pressure to improve locomotor rehabilitation, the limb will apply some reaction force to compression.

Oehler *et al.* [15] focuses on design optimization of shape memory alloy (SMA) morphing structures and builds on the work of Hartl *et al.* [16] who focus on design optimization of SMA-based aerostructures. Oehler *et al.* finds that, because simple gradient-based algorithms are sensitive to missing data and have difficulty converging when this occurs, a Design Explorer tool suite algorithm developed by Boeing is useful to overcome such challenges [15]. They note that while their model is suitable for optimization with genetic algorithms, GAs were overlooked due to the high number of runs necessary to achieve convergence.

A shape matching approach was developed initially by Murray *et al.* for rigid link mechanisms [17]. Analytical modeling of segmented unimorphs was conducted by Frecker and Aguilera [18]. This analytical modeling was used to find the deflections of a functionally graded compliant mechanism and then optimized by Jovanova *et al.* [19,20].

The analytical modeling of a segmented unimorph that Frecker and Aguilera [18] develop is extended in previous work by the authors [7]. Using this extended analytical modeling, shape matching can be conducted using a genetic algorithm.

1.4. Genetic algorithms

Genetic algorithms (GA) are based on Darwin's evolutionary principles, where individual attributes determine the fitness of a particular individual or design. This fitness function is used as the objective function that is minimized in GAs. Thus 'best fitness' is defined as the design with the lowest fitness function of the population analyzed. The attributes that are used to determine the best fitness are defined as genes.

The most beneficial attributes (genes) or design variables in this case, may move on or be combined generation to generation and may live on to see the final generation. Thus, with a random first generation with a sufficiently large initial population, an optimal design may be generated. An introduction to GA can be found in work by Mitchell [21].

Genetic algorithms are different from gradient-based optimization methods in the role random choices play in each new generation. The introduction of randomness allows a more thorough exploration of the parameter space than gradient-based methods such as iterated hill-climbing methods [21]. Mitchell notes that for GAs to function well and approach an idealized genetic algorithm (IGA), several factors are necessary. Samples must be independent (large enough population, slow enough selection process, and sufficiently high mutation rate), schemas must be sequestered successfully (desired schemas should be preserved), and crossover should be effectively instantaneous (the time for two schemas to crossover must be much smaller than the time to discover the schemas) [21]. They also note the GA should have speedup compared to Random-Mutation Hill Climbing (RMHC). RHMC is a form of systematic design exploration that loses virtually no designs to mutations, whereas GA can be a rapid design exploration that may miss optimal designs and as such crossover rates should be carefully considered to speed up the GA relative to RHMC, but still maintain successfully sequestered desired schema. Speedup is just one benefit of GAs.

The benefits of the native MATLAB genetic algorithm toolbox are discussed in depth by Bhargava *et al.* [22] and summarizes as ease of use and experimentation.

Chand and Dutta [23] perform a shape optimization of structures subjected to transient dynamic loading using genetic algorithms. They integrate automatic mesh generation and adaptive FEA modules with a GA code. They present case studies on the response of a cantilever beam suddenly subjected to applied loading at the free end and the response of a simply supported beam subjected to a transient step loading in the middle.

Rietz and Peterson [24] conduct a simultaneous shape and thickness optimization using an optimality criteria method. This method is the foundation of a more common optimization technique found in topology optimization as covered by Bendsøe [25] in their 1995 work.

2. METHODS

The analytical model used is described in detail in previous work by the authors [7], but is introduced in brief here. The free deflection of a unimorph [7], or bimorph [14] LIB actuator is found by solving the quasistatic equations of equilibrium to get the free curvature from the introduction of some actuation strain that is induced through battery charging.

The free curvature is used to calculate the local deflections of finite elements along the length of the actuator. These local deflections are transformed into global coordinates to get the free deflection that is used to predict the actuated shapes shown in this paper.

2.1. Design optimization problem formulation

A schematic for an N-layer, N-segment bimorph can be seen in Figure 1, where the white lines denote the split between electrically isolated and mechanically connected segments. Assuming electric isolation between segments allows each segment to maintain separate SOC, while mechanical connection allows continuous deflection along the length of the segmented actuator.

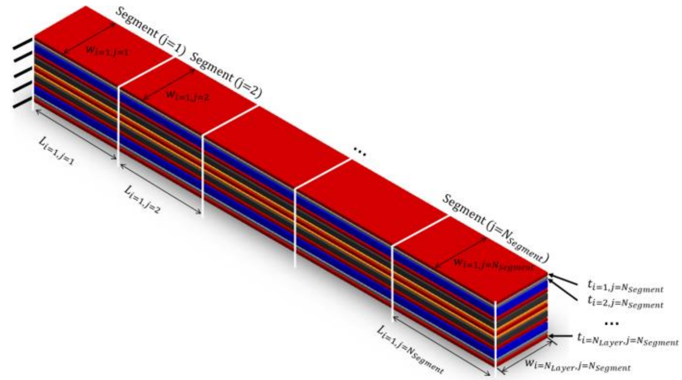

Figure 1. Schematic for an N_{Layer}, $N_{Segment}$ multilayer actuator

1D shape matching allows for the intelligent design of a segmented actuator to achieve a particular shape while subject to various constraints. The objective function is adapted from work by Jovanova *et al.* where shape matching is used for a 1D functionally graded material beam [19].

For gp number of specified points, the shape matching error ($\Delta_{e_{1D}}$) is defined in equation (1) as the summed root mean squared error (RMSE) between a set of points that define a target shape and a set of points that describes the actuated shape. The actuated shape is defined by a pseudo-random set of design variables generated by a GA. Figure 2 highlights an example target shape schematic where the undeformed shape, actuated shape, target shape, and *gp* specified reference points are shown. For *gp* number of specified points, the shape error ($\Delta_{e_{1D}}$) is calculated as:

$$\Delta_{e_{1D}} = \sum_{n=1}^{gp} \Delta_{en} \tag{1}$$

where Δ_{en} is the root mean squared error (RMSE) as shown in equation (2).

$$\Delta_{e_n} = \sqrt{\left[\left(X_{act} - X_{target}\right)^2 + \left(Y_{act} - Y_{target}\right)^2\right]} \tag{2}$$

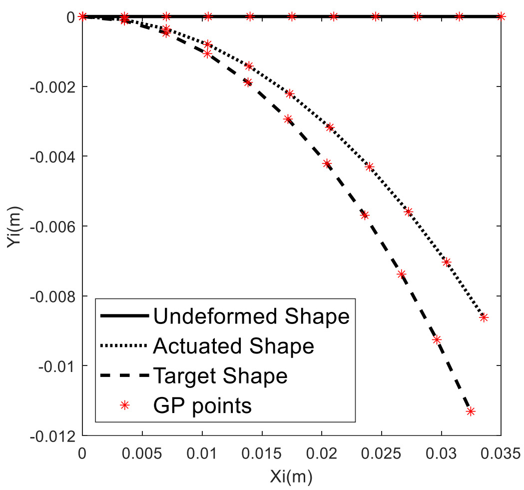

Figure 2. Target shape schematic

A shape matching design optimization problem, where the objective is to minimize shape error between the actuated shape and target shape is defined in equation (3).

$$Minimize\ (f_1)$$

where,

$$f_1 = \sum_{n=1}^{gp} \Delta_{e_n}\ [19] \tag{3}$$

$$x_{lower\_bound} \leq x \leq x_{upper\_bound}.$$

X_{act} and Y_{act} refer to the longitudinal and transverse deflection points of the actuated shape and X_{target} and Y_{target} refer to the longitudinal and transverse deflection of the target shape for gp points. The shape matching error ($\Delta_{e_{1D}}$) is minimized. The design variables (x) are bounded above and below by x_{lower_bound} and x_{upper_bound}.

Notably, to improve the accuracy of the problem, the 'best' X_{act} is chosen against the available X_{target} points. Because the target data points may be limited and the potential points generated for the model is infinite, many deflection points are generated for the model to compare the target data points against. The X_{act} point that is closest to each X_{target} point is chosen, such that the respective Y_{act} and Y_{target} data points can be compared. As such, the $\left(X_{act} - X_{target}\right)^2$ term is much smaller than the $\left(Y_{act} - Y_{target}\right)^2$ term. The analytical model used to generate the deflections can be found in previously published work [7].

2.2. Assumptions

Due to the relatively quick propagation of lithium through silicon (~0.4hr for silicon particles on the order of tens to hundreds of nanometers in diameter) relative to the charging rates of LIBS (20hr for C/20 charge rate), lithiation (and actuation) is assumed to be quasistatic [7]. While actuation strain may vary nonlinearly with SOC, the relationship between actuation strain and SOC is assumed to be linear for simplicity. All segments are electrically isolated and mechanically connected to allow for different SOC between segments and continuous bending. All materials are considered linearly elastic and isotropic due to the high aspect ratio. The actuator length is several orders of magnitude larger than the thickness and nearly one order of magnitude greater than the actuator width. Self-weight is considered negligible due to the relatively small effect weight would contribute to the bending moment compared to the moment due to induced actuation strain.

2.3. Solution methods

A native genetic algorithm solver in MATLAB (GA) is used to minimize the shape error. All options (*e.g.,* population size, crossover rate, etc.) are default unless specified otherwise in the corresponding case study.

3. RESULTS AND DISCUSSION

3.1. Case study 1: Notched unimorph

The first case study investigated is an experimentally validated notched unimorph configuration shown in Figure 3. The experimental data serves as the target shape. The shape matching of the experimental data target shape allows for validation of this approach. Actuation strain S_1^* is defined in equation (4) as proportional to the state of charge or SOC with the proportional constant being defined as an effective linear strain constant β_{eff}. SOC ranges from zero to one, or uncharged to fully charged. The actuation strain of each segment is the set of design variables (x).

$$S_1^* = \beta_{eff} SOC \tag{4}$$

$$0 \leq SOC \leq 1 \tag{5}$$

Shan *et al.* conduct an experiment with the notched unimorph configuration and predict a uniform SOC=23% throughout the length of the unimorph [26]. Shan *et al.* capture the free deflection of the notched unimorph every 3 minutes with a macro-lens digital camera. A previous study has shown a β_{eff}=17% [13], but for the sake of simplicity we assume that $\beta_{eff} = 100\%$ and optimize for actuation strain such that $S_1^* = SOC$.

However, an assumed effective linear strain constant can guide the upper bound of actuation strain for the design optimization. For β_{eff}=17%, $S_{i=1}^* = 3.91\%$ and therefore an upper bound of actuation strain of $S_{i=1}^* = 10\%$ should be reasonable and will allow for a narrower population range. A narrower range of population will allow for a more thorough exploration of the design space and potentially better shape matching.

The experiment consists of a transparent battery system originally developed by Ma *et al.* [9] whereby a macro-lens digital camera is used to capture deflection data along the length of the unimorph. The images captured undergo image processing to procure the experimental deflection points for multiple SOC. However, the target shape used is for a single SOC=23%. It is important to note the geometry of the notched unimorph.

From the top (fixed) to the bottom (free) the notched unimorph consists of three geometric segments. This is summarized in Table 1.

Table 1. Geometric parameters and material properties for notched unimorph configuration.

Segment thicknesses ($t_{i,j}$) (μm)	$i = 1$ Coating layer	$i = 2$ Copper foil	$i = 3$ Tape
$j = 1$	36	9	30
$j = 2$	36	9	0
$j = 3$	36	9	30
Segment elastic moduli ($E_{i,j}$) (GPa)	$i = 1$ Coating layer	$i = 2$ Copper foil	$i = 3$ Tape
$j = 1$	1[9]	120	1.5
$j = 2$	1[9]	120	1.5
$j = 3$	1[9]	120	1.5
Length ($L_{i,j}$) (cm)	All layers ($i = 1{:}3$)		
$j = 1$	1.5		
$j = 2$	0.5		
$j = 3$	1.5		
Width ($w_{i,j}$) (mm)	All layers ($i = 1{:}3$)		
$j = 1$	5		
$j = 2$	5		
$j = 3$	5		

The population is set to 100, and the convergence tolerance is set to 1e-6 to ensure good starting diversity and good shape matching results when converged.

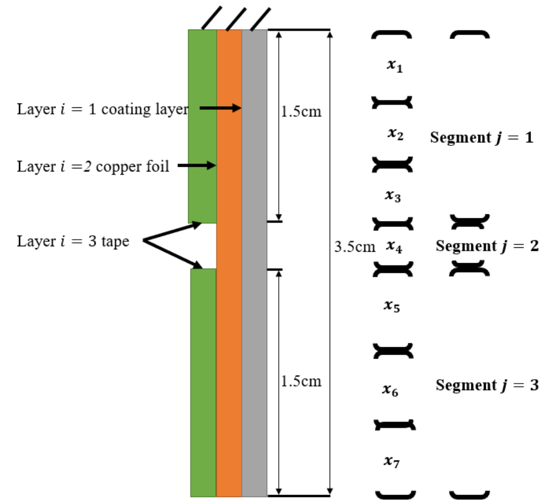

Figure 3. Schematic for the distribution of design variables (x) throughout a three segment notched unimorph configuration.

It is important to note that segment one and segment three have three design variables each to ensure that the length (0.5cm) over which each actuation strain is applied is uniform.

A 3-segment model (with seven total design variables) is used to match the target shape set out by the experiment. The unimorph is split into seven subsegments (each with their own design variable) of uniform length $L_{j=1:7} = 0.5cm$. Subsegments here are used to describe the smaller portions of each segment over which the design variables (actuation strain) are varied. Recall, the length of the notch (and the smallest geometric variation) is 0.5cm. As seen in Figure 4, good shape matching is achieved. Here, the only design variable varied is the S_i^* (actuation strain).

The convergence plot is shown in Figure 5. The shape matching error that results from this is $\Delta_{e_{1D}} = 512\mu$m. An optimal actuation strain distribution throughout the seven-segment notched unimorph is shown in Table 2. The expected result for a notched unimorph that is uniformly actuated is that there should be significantly more curvature in the more compliant notch (segment 2). This is only somewhat true for the optimal actuation strain distribution shown.

Subsegments 2 and 6 are effectively unactuated. The largest actuation strains seen are in subsegments 1, 3, 4, 5, and 7. The largest of these is found in subsegment 7 with only 0.15% strain. The second largest actuation strain is throughout the notch and the adjoining subsegments for $S_{i=1,j=3:5}^*$. These actuation strains vary from 0.08% to 0.10% strain, where the compliance is highest.

It is worth noting that the best fitness is defined here as the lowest value among the population at a given generation and the mean fitness is the average fitness of the population at the same generation.

The design optimization minimizes the shape error between the actuated shape predicted by the model and the target shape, however the battery in the experiment appears to be relatively uncharged and therefore has a very small actuation strain. This is thought to be due to a lack of charging along the length of the beam and a concentration of lithium at the base of the beam. The closer the cathode and anode are, as occurs at the base, the more preferentially it is thought that lithiation occurs, such that as the tip of the anode deflects further from the cathode, it becomes less lithiated.

The relatively larger actuation strain at the tip is thought to be due to widely spread experimental data points. The reason for the lack of perfect overlay is due to twisting in the unimorph that occurs in the experiment. To account for the twisting, the average deflection of both sides of the unimorph is used as the target shape. However, the twisting is thought to be responsible for the poor matching in places.

Table 2. Optimal design variables for notched unimorph configuration

Segment for layer $i = 1$	Actuated actuation strain (%)	Target actuation strain (%)	Total Shape Error (μm)
$j = 1$	0.1	3.91	51.2
$j = 2$	0.00	3.91	
$j = 3$	0.10	3.91	
$j = 4$	0.08	3.91	
$j = 5$	0.10	3.91	
$j = 6$	0.00	3.91	
$j = 7$	0.15	3.91	

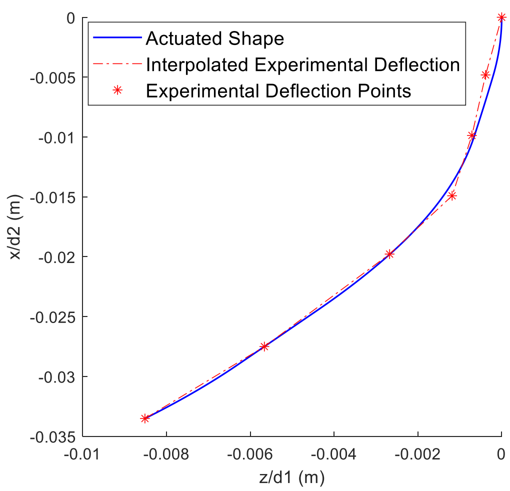

Figure 4. Optimal shape matching of a 3-layer, 7-subsegment notched unimorph model

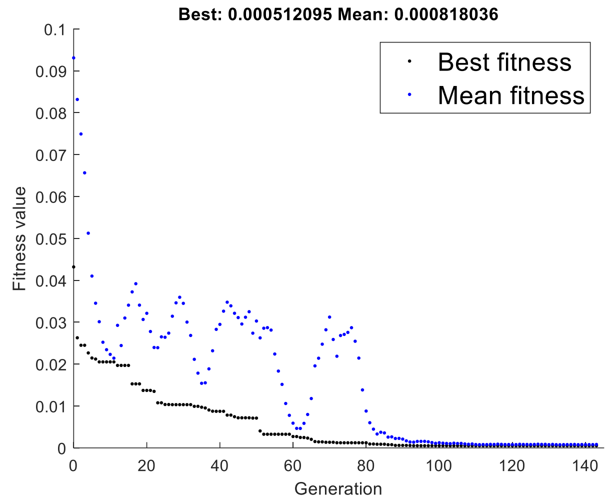

Figure 5. Convergence plot for optimal shape matching of a 3-layer, 7-subsegment notched unimorph model

3.2. Case Study 2: Tapered five-segment unimorph

In Case Study 2 the design variables are the copper foil passive layer segment thicknesses while the actuation strain is held constant. The constraints on the design variables are shown in equation (6). This allows for the variation of passive layer thickness for each of five segments. Shown in Figure 1, a 13-layer, five-segment beam is optimized against a target shape shown in Figure 6. Notably, there are two copper foil passive layers, and both are set equal to the thicknesses randomly generated by the GA.

$$Minimize\ (f_1)$$

where,

$$f_1 = \sum_{n=1}^{gp} \Delta_{e_n} \ [19] \tag{6}$$

$$10\mu m \leq t_{i=6,8,j} \leq 34\mu m.$$

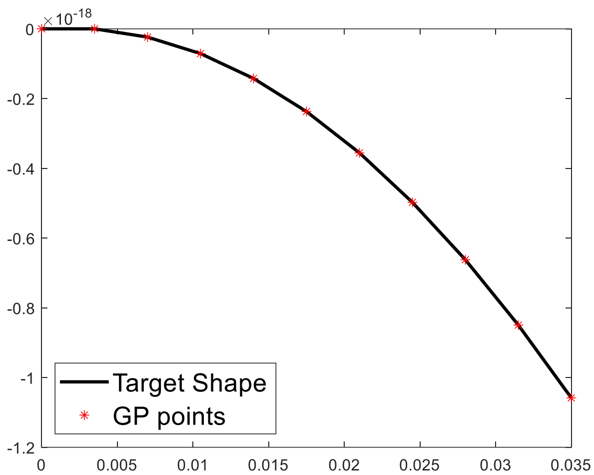

Figure 6. 13-layer, 5-segment unimorph target shape

The target shape is derived from the free deflection a tapered, thirteen-layer, five-segment lithium ion battery unimorph undergoes at full charge. The equations necessary to predict the free deflection are found in previous work [7]. The geometric parameters and material properties of the multilayer are shown in Table 3.

Table 3. Geometric parameters and material properties for a tapered 13-layer, 5-segment unimorph.

All segments $j = 1{:}5$	Separator 1,4,7,10,13	Al 2,12	NCM 3,11	Si 5,9	Cu 6,8
Thicknesses $(t_{i,j})$ (μm)	20	15	44	19	N/A
Elastic moduli $(E_{i,j})$ (GPa)	0.1247	70	1.5	1 [9]	120
Width $(w_{i,j})$ (mm)	8	6	6	4	4
Length $(L_{i,j})$ (cm)	0.7				

The best shape error is found to be $\Delta_{e_{1D}} = 3\mu m$. An optimal shape is shown overlaid over the target shape in Figure 7 with the convergence plot shown in Figure 8. Partial convergence occurs in less than 20 generations, but the algorithm takes until just over 50 generations to fully converge due to the relatively small convergence tolerance. Based on the values shown in Table 4, the actuated shape approaches the set design variables of the target shape. There is no more than $1\mu m$ of divergence from the target shape in any segment.

Table 4. Optimal design variables for a tapered, 13-layer, 5-segment unimorph

Segment for layer $i = 6{,}8$	Actuated shape passive layer thickness (μm)	Target shape passive layer thickness (μm)	Total shape error $(\mu$m)
$j = 1$	33.54	34	2.9
$j = 2$	27.37	28	
$j = 3$	22.29	22	
$j = 4$	15.21	16	
$j = 5$	10.87	10	

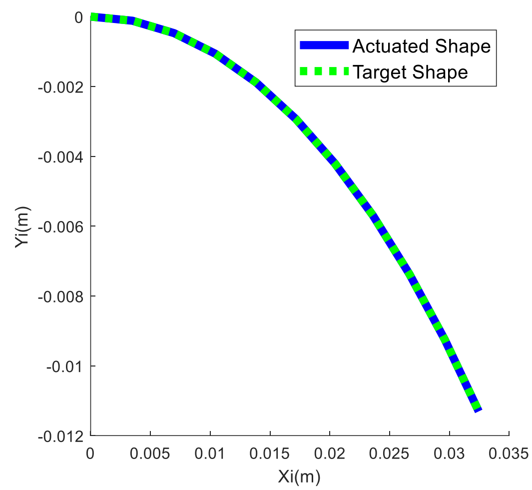

Figure 7. Optimal shape matching for a 13-layer, 5-segment unimorph against a tapered actuator target shape

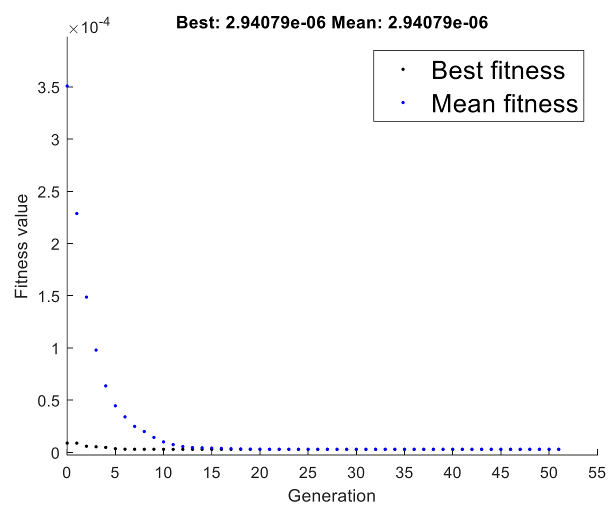

Figure 8. Convergence plot for shape matching of a tapered 13-layer, 5-segment unimorph

3.3. Case Study 3: Alternating SOC bimorph

A third case study uses the same 13-layer schematic shown in Figure 1, but extended into an 8-segment long configuration.

Whereas in case study 2, only the top active silicon coating layer is actuated, both the top and bottom layer are activated in this bimorph case study. The target shape alternates top layer and bottom active layer activation as described in Table 5. The design variables are the actuation strains of the top and bottom active layer of each segment. The problem formulation is shown in equation (7).

$$Minimize\ (f_1)$$

where,

$$f_1 = \sum_{n=1}^{gp} \Delta_{e_n}\ [19] \qquad (7)$$

$$0 \leq S^*_{i=5,j=1} \leq 64\%$$
$$0 \leq S^*_{i=9,j=1} \leq 64\%.$$

A shape error of $\Delta_{e_{1D}} = 48.8\mu m$ is found after convergence in nearly 70 generations as shown in Figure 10. The design variables are shown in Table 5 for both the actuated shape and the target shape. Notably, the difference between the actuation strain of the top active layer and bottom active layer approaches the actuation strain of the activated active layer in the target shape.

For example, the differential actuation strain (difference in actuation strain between the top and bottom active layers) of segment 1 is: $S^*_{i=5,j=1} - S^*_{i=9,j=1} = 127.9 - 65.8 = 62.1\%$. The target actuation strain of the top active layer of segment 1 is 64%. The same pattern is true along the length of the beam.

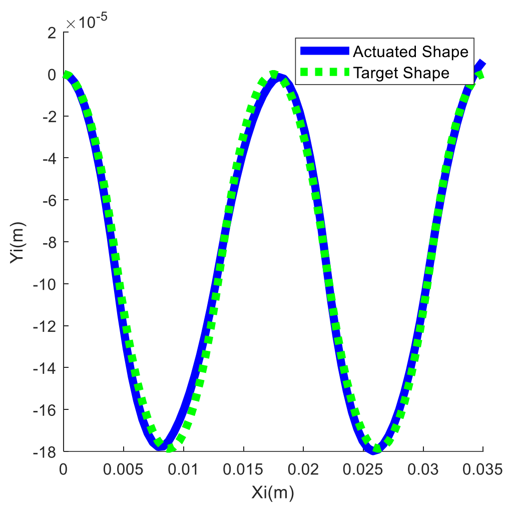

Figure 9. Optimal shape matching for an 8-segment alternating SOC bimorph

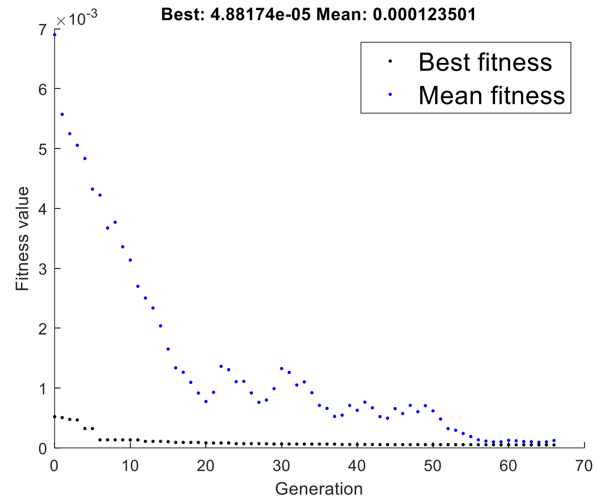

Figure 10. Convergence plot for shape matching of an 8-segment alternating SOC bimorph

Table 5. Optimal design variables for an 8-segment alternating SOC bimorph

Segment	Top active layer actuation strain for layer $i = 5$ (%)		Top bottom layer actuation strain for layer $i = 9$ (%)		Total Shape Error (µm)
	Actuated Shape	Target shape	Actuated Shape	Target shape	
$j = 1$	127.9	64	65.8	0	48.8
$j = 2$	10.5	0	72.1	64	
$j = 3$	50.8	0	109.4	64	
$j = 4$	127.1	64	77.4	0	
$j = 5$	124.0	64	43.0	0	
$j = 6$	30.9	0	109.3	64	
$j = 7$	27.4	0	82.6	64	
$j = 8$	91.7	64	35.1	0	

4. CONCLUSION

Good target shape matching is achieved through the implementation of a GA solver. Shape matching error is found to range from 0.029% of the length ($\Delta_{e_{1D}} = 3\mu m$) to 1.5% ($\Delta_{e_{1D}} = 512\mu m$). Three case studies are examined.

The first case study involves the shape matching of an experimental notched unimorph with the actuation strain of seven subsegments as the design variables. An objective function value of $\Delta_{e_{1D}} = 512\mu m$ is found for the notched unimorph. The shape error found is 1.5% of the length.

Case study 1 is used to inform improved experimental design. Notably, the current design appears have a concentration of lithiation at the base and appears to be more than an order of magnitude off from the anticipated actuation strain expected from the experimental design. It is concluded that the LIB actuator is either receiving less charge than expected or is substantially stiffer than estimated by the given parameters.

A second tapered unimorph case study is investigated with segmented passive layer thickness as the design variables. The target shape matched against is a tapered unimorph actuator at full charge taken from previous modeling work [7]. Good shape matching is achieved ($\Delta_{e_{1D}} = 3\mu m$) and not only is the taper of the beam maintained, but the resulting passive layer thickness matches the target shape within $1\mu m$ for every segment. A shape error is found to be 0.029% of the length. The conclusion reached here is that unimorph actuation is simpler to optimize due to the reduced number of design variables, but is restricted to either convex or concave actuation.

The third case study involves the optimization of an 8-segment bimorph where design variables of both the top and bottom active layer actuation strain are simultaneously varied. Good shape matching is achieved ($\Delta_{e_{1D}} = 48.8\mu m$, 0.23% of the length) and it is found that simultaneously varying the actuation strain allows for infinitely many solutions, but that the differential actuation strain between top and bottom active layer is effectively the actuation strain of the activated layer set in the target shape.

The overall conclusion reached by this paper is that a LIB actuator can be optimized to achieve tailorable, complex shapes with both concave and convex curvature. Additional stored energy can be drained by an external circuit or redistributed internally without affecting the free deflection. The possibilities for this technology include remote, off-the-grid applications as the soft robotic actuators can be initially charged on-site and transported off-site to a location where work must be done.

Future work could consist of more complex shape case studies for bimorph and multimorph models. Focusing on investigating a multi-objective function that minimizes active material volume or maximizes blocked force while simultaneously minimizing shape error would also improve upon the work performed here.

ACKNOWLEDGEMENTS

The authors gratefully acknowledge the support of the National Science Foundation under Grant No. 1662055.

REFERENCES

[1] Goodenough, J. B., and Park, K. S., 2013, "The Li-Ion Rechargeable Battery: A Perspective," J. Am. Chem. Soc., **135**(4), pp. 1167–1176.

[2] Rahn, C. D.; Wang, C. Y., 2013, *Battery Systems Engineering*, John Wiley & Sons.

[3] Yao, Y., Huo, K., Hu, L., Liu, N., Cha, J. J., McDowell, M. T., Chu, P. K., and Cui, Y., 2011, "Highly Conductive, Mechanically Robust, and Electrochemically Inactive TiC/C Nanofiber Scaffold for High-Performance Silicon Anode Batteries," ACS Nano, **5**(10), pp. 8346–8351.

[4] Chin, T. E., Rhyner, U., Koyama, Y., Hall, S. R., and Chiang, Y.-M., 2006, "Lithium Rechargeable Batteries as Electromechanical Actuators," Electrochem. Solid-State Lett., **9**(3), p. A134.

[5] Baranchugov, V., Markevich, E., Pollak, E., Salitra, G., and Aurbach, D., 2007, "Amorphous Silicon Thin Films as a High Capacity Anodes for Li-Ion Batteries in Ionic Liquid Electrolytes," Electrochem. commun., **9**(4), pp. 796–800.

[6] Liu, X. H., Zhong, L., Huang, S., Mao, S. X., Zhu, T., and Huang, J. Y., 2012, "Size-Dependent Fracture of Silicon Nanoparticles during Lithiation," ACS Nano, **6**(2), pp. 1522–1531.

[7] Gonzalez, C., Ma, J., Frecker, M., and Rahn, C., 2021, "Analytical Modeling and Simulation of a Multifunctional Segmented Lithium Ion Battery Unimorph Actuator," Smart Mater. Struct., **30**(1), p. 015039.

[8] Cannarella, J., Leng, C. Z., and Arnold, C. B., 2014, "On the Coupling between Stress and Voltage in Lithium-Ion Pouch Cells," *Energy Harvesting and Storage: Materials, Devices, and Applications V*, N.K. Dhar, P. Balaya, and A.K. Dutta, eds., p. 91150K.

[9] Ma, J., Gonzalez, C., Huang, Q., Farese, J., Rahn, C., Frecker, M., and Wang, D., 2020, "Multifunctional Li(Ni 0.5 Co 0.2 Mn 0.3) O 2 -Si Batteries with Self-Actuation and Self-Sensing," J. Intell. Mater. Syst. Struct., **31**(6), pp. 860–868.

[10] Ma, J., Gonzalez, C., Rahn, C., Frecker, M., and Wang, D., 2018, "Experimental Study of Multifunctional NCM-Si Batteries With Self-Actuation," *Volume 1: Development and Characterization of Multifunctional Materials; Modeling, Simulation, and Control of Adaptive Systems; Integrated System Design and Implementation*, American Society of Mechanical Engineers, San Antonio, Texas, USA.

[11] Ma, J., Rahn, C., and Frecker, M., 2017, "Multifunctional NMC-Si Batteries With Self-Actuation and Self-Sensing," *Volume 1: Development and Characterization of Multifunctional Materials; Mechanics and Behavior of Active Materials; Bioinspired Smart Materials and Systems; Energy Harvesting; Emerging Technologies*, American Society of Mechanical Engineers, Snowbird, Utah, USA.

[12] Gonzalez, C., Ma, J., Frecker, M., and Rahn, C., 2018, "Analytical Modeling of a Multifunctional Segmented Lithium Ion Battery Unimorph Actuator," *Volume 2: Mechanics and Behavior of Active Materials; Structural Health Monitoring; Bioinspired Smart Materials and Systems; Energy Harvesting; Emerging Technologies*, American Society of Mechanical Engineers, San Antonio, Texas, USA.

[13] Gonzalez, C., Ma, J., Frecker, M., and Rahn, C., 2019, "Analytical Modeling and Simulation of the Blocked Force and Large Deformation of Multifunctional Segmented Lithium Ion Battery Unimorph Actuator," *ASME 2019 Conference on Smart Materials, Adaptive Structures and Intelligent Systems*, American Society of Mechanical Engineers, Louisville, KT.

[14] Gonzalez, C., Shan, S., Frecker, M., and Rahn, C., 2020, "Analytical Modeling of a Segmented Bimorph Lithium

Ion Battery Actuator," *ASME 2020 Conference on Smart Materials, Adaptive Structures and Intelligent Systems*, American Society of Mechanical Engineers.

[15] Oehler, S. D., Hartl, D. J., Lopez, R., Malak, R. J., and Lagoudas, D. C., 2012, "Design Optimization and Uncertainty Analysis of SMA Morphing Structures," Smart Mater. Struct., **21**(9).

[16] Hartl, D. J., Lagoudas, D. C., and Calkins, F. T., 2011, "Advanced Methods for the Analysis, Design, and Optimization of SMA-Based Aerostructures," Smart Mater. Struct., **20**(9).

[17] Murray, A. P., Schmiedeler, J. P., and Korte, B. M., 2008, "Kinematic Synthesis of Planar, Shape-Changing Rigid-Body Mechanisms," J. Mech. Des. Trans. ASME, **130**(3), pp. 1–10.

[18] Frecker, M. I., and Aguilera, W. M., 2004, "Analytical Modeling of a Segmented Unimorph Actuator Using Electrostrictive P(VDF-TrFE) Copolymer," Smart Mater. Struct., **13**(1), pp. 82–91.

[19] Jovanova, J., Frecker, M., Hamilton, R. F., and Palmer, T. A., 2019, "Target Shape Optimization of Functionally Graded Shape Memory Alloy Compliant Mechanisms," J. Intell. Mater. Syst. Struct., **30**(9), pp. 1385–1396.

[20] Jovanova, J., Frecker, M., Hamilton, R. F., and Palmer, T. A., 2016, "Target Shape Optimization of Functionally Graded Shape Memory Alloy Compliant Mechanism," *Volume 2: Modeling, Simulation and Control; Bio-Inspired Smart Materials and Systems; Energy Harvesting*, American Society of Mechanical Engineers.

[21] Mitchell, M., 1998, "An Introduction to Genetic Algorithms (Complex Adaptive Systems)," MIT Press.

[22] Bhargava, P. N., 2018, "MULTIDIMENSIONAL ANALYSIS OF GENETIC ALGORITHM USING MATLAB," Int. J. Adv. Res. Comput. Sci., **9**(2), pp. 554–558.

[23] Chand, S., and Dutta, A., 2005, "Reliable Shape Optimization of Structures Subjected to Transient Dynamic Loading Using Genetic Algorithms," Shock Vib., **12**(6), pp. 407–424.

[24] Rietz, A., and Petersson, J., 2001, "Simultaneous Shape and Thickness Optimization," Struct. Multidiscip. Optim., **23**(1), pp. 14–23.

[25] Bendsøe, M. P., 1995, *Optimization of Structural Topology, Shape, and Material*, Springer Berlin Heidelberg, Berlin, Heidelberg.

[26] Shan, Shuhua; Gonzalez, C. C. R. F. M., 2021, "EXPERIMENTAL STUDY OF NCM-SI BATTERIES WITH BIMORPH ACTUATION," *ASME 2021 Conference on Smart Materials, Adaptive Structures and Intelligent Systems*, Unpublished, Virtual.